Quantitative in situ synchrotron X-ray analysis of the ALD/MLD growth of transition metal dichalcogenide TiS2 ultrathin films

A. Yadav, W. Ma, P. Abi Younes, G. Ciatto, N. Gauthier, E. Skopin, E. Quadrelli, N. Schneider, H. Renevier

Nanoscale

PAPER

View Article Online
View Journal | View Issue

Cite this: *Nanoscale*, 2024, **16**, 1853

Quantitative *in situ* synchrotron X-ray analysis of the ALD/MLD growth of transition metal dichalcogenide TiS_2 ultrathin films†

Ashok-Kumar Yadav, *[a] Weiliang Ma, [b] Petros Abi Younes, [c,d] Gianluca Ciatto, *[a] Nicolas Gauthier, [d] Evgeniy Skopin, [c] Elsje Alessandra Quadrelli, [e] Nathanaelle Schneider [b] and Hubert Renevier [c]

Received 22nd August 2023,
Accepted 11th December 2023

DOI: 10.1039/d3nr04222g

rsc.li/nanoscale

We present the results of a full quantitative analysis of X-ray absorption spectroscopy (XAS) performed *in situ* during the growth of ultrathin titanium disulfide (TiS_2) films *via* an innovative two-step process, *i.e.* atomic layer deposition/molecular layer deposition (ALD/MLD) followed by annealing. This growth strategy aims at separating the growth process from the crystallization process by first creating an amorphous Ti-thiolate that is converted later to crystalline TiS_2 *via* thermal annealing. The simultaneous analysis of Ti and S K-edge XAS spectra, exploiting the insights from density functional theory calculations, allows us to shed light on the chemical and structural mechanisms underlying the main steps of growth. The nature of the bonding at the base of the interface creation with the SiO_2 substrate is disclosed in this study. Evidence of a progressive incorporation of S in the amorphous Ti-thiolate is given. Finally, it is shown that the annealing step plays a critical role since the transformation of the Ti-thiolate into nanocrystalline TiS_2 and the loss of S are simultaneously induced, validating the two-step synthesis approach, which entails distinct growth and crystallization steps. These observations contribute to a deeper understanding of the bonding mechanism at the interface and provide insights for future research in this field and the generation of ultra-thin layered materials.

Introduction

Transition metal dichalcogenides (TMDs) have been receiving great interest over the past few years due to their potential future applications in super-capacitors, batteries, electronics, and optoelectronics.[1,2] Lamellar titanium disulfide TiS_2, which consists of S–Ti–S layers separated by van der Waals gaps, is also considered to be integrated into emerging energy devices such as rechargeable batteries due to its kinetically favorable insertion reaction with alkali metals.[3–6] The good electrical conductivity, high energy density and rapid cycling rate of TiS_2 make it a strong contender as an electrode in lithium-ion batteries as well as for applications in high-power systems.[7–10] However, ultra-thin films of TiS_2 are technologically challenging to prepare on a large scale for device applications. The top-down approach (mechanical exfoliation) for generating ultrathin or monolayer TiS_2 is ineffective for scalable applications due to a lack of precise control over the number of layers, crystal quality, and lateral dimension of grains.[11,12]

Among the various bottom-up growth methods, atomic layer deposition (ALD) could produce high-quality thin films of TiS_2 in a controlled manner.[13–17] The ultrathin films prepared by ALD bring about new challenges due to the anisotropy of TMDs coupled with extreme thinness. Various efforts have been made such as post-annealing or chalcogenization of ALD-grown transition metal oxides;[13–15,18] however, controlling the reaction parameters to obtain the predetermined crystal structure remains a challenge due to the co-occurrence of growth and crystallization during the ALD process. This can be controlled to some extent using specific crystalline substrates with adequate lattice parameters.[19] The alternative approach, which has a larger substrate scope and has been successfully demonstrated by some of us for MoS_2, is

[a]*Synchrotron SOLEIL, Beamline SIRIUS, Saint-Aubin, F-91192 Gif sur Yvette, France. E-mail: gianluca.ciatto@synchrotron-soleil.fr, ashok-kumar.yadav@synchrotron-soleil.fr*
[b]*IPVF (UMR 9006), Institut Photovoltaïque d'Ile-de-France, F-91120 Palaiseau, France*
[c]*Univ. Grenoble Alpes, CNRS, Grenoble-INP, LMGP, F-38000 Grenoble, France*
[d]*Univ. Grenoble Alpes, CEA, LETI, F-38000 Grenoble, France*
[e]*Université de Lyon, IRCELYON (UMR 5256, CNRS and Université de Lyon1), F-69100 Villeurbanne, France*

† Electronic supplementary information (ESI) available: Methodologies for XAFS analysis, linear combination fitting, amorphous TiS_2 XANES simulation and quantitative determination of bond lengths and interatomic distances *via* XAS. See DOI: https://doi.org/10.1039/d3nr04222g

to completely dissociate deposition and crystallization by using organic precursors during the ALD process.[20] Two parent gas-phase thin-film techniques, ALD for inorganic materials (metal oxides, sulfides, and nitrides)[21] and its counterpart, molecular layer deposition (MLD) for purely organic thin films (*e.g.*, polyimides and polyamides),[22,23] have been combined as ALD/MLD.[24,25] The bridging of flexible organic chemical residues between the layers prevents crystallization during the growth of the hybrid inorganic–organic thin film at low temperatures and a post-treatment ensures the removal of the organic part, which leads to the crystallization of the required phase.[26,27] This ALD/MLD + annealing strategy has been used to produce atomically thin MoS_2-based layers oriented parallel to the substrate.[20] Very recently, we have proved the controlled growth of TiS_2 ultra-thin films by a two-step process composed of (i) the ALD/MLD step using inorganic and organic precursors (tetrakis-dimethylamido titanium (TDMAT) and 1,2-ethanedithiol (EDT)) and (ii) annealing under an Ar/H_2 atmosphere.[28]

The continuous development of the preparation of ultrathin films of TiS_2 with controlled size and structure relies on a deep understanding of ALD/MLD and requires multi-characterization. The kinetics of every conceivable growth reaction and side reaction for a given system should be evaluated for better understanding and control of the process. Clearly, this is rarely possible looking at the complexity of the reactions, but fortunately, some of the initial and final steps can be deconvoluted using various structural and chemical techniques. Understanding some of the selected key reaction steps may be sufficient to answer specific questions about a process. A notable chemical technique involves simulating experimental conditions on high-surface area silica beads to serve as a representative model for a flat wafer substrate.[29–32] Due to the similarities in the chemical nature of the reactive sites and site density between the two, the silica bead model has been effectively utilized by our group in employing spectroscopic and analytical tools to demonstrate the analogy beyond the first pulse and successfully model the whole ALD/MLD growth process of TMD phases.[20,28] Besides, synchrotron radiation has emerged as a valuable tool for facilitating *in situ* X-ray-based studies during ALD/MLD, particularly for examining the growth process from its initial cycles. This is due to the brilliance of the X-ray flux provided by synchrotrons and their exceptional capability to tune the photon energy to match specific experiments and material systems.[20,33–35]

In situ X-ray absorption spectroscopy (XAS) is a powerful tool for studying ALD/MLD processes due to several key advantages. One of the most important advantages is its element specificity, allowing it to provide detailed information about the local structure surrounding probe elements such as titanium and sulfur. Unlike some other techniques, XAS is well-suited for characterizing non-crystalline or poorly crystalline samples, which is crucial in ALD/MLD processes where well-defined crystalline structures are often lacking, especially during growth. *In situ* XAS is highly sensitive and capable of detecting trace amounts of probe elements. This sensitivity is particularly valuable for monitoring the early stages of ALD/MLD growth when only a few probe elements are present on the substrate surface. Additionally, it can track changes in the oxidation state of the probe elements during the deposition process, and it is sensitive to the entire thickness of the deposited layers.

In this present work, we introduce two novel cross-talking analysis elements to gain deeper insight into the chemistry and structure of selected steps of the TiS_2 ALD/MLD: a full quantitative analysis of the X-ray absorption spectroscopy (XAS) data collected *in situ* and modelling of the ALD/MLD process using density functional theory (DFT). DFT modeling allows one to calculate the pathways for precursor adsorption, ligand migration, and by-product formation on the surface, yielding reaction energies and activation energies for each step and indicating whether the reaction is thermodynamically or kinetically favorable at the temperature of interest.[36,37] It also provides us with possible structures from which XAS spectra can be simulated and compared with the *in situ* experimental results, determining the bonding behavior of the precursor with the surface in the early stages.[38] XAS, being an element-selective and local structure technique, allows us to probe the evolution of each ALD/MLD growth cycle in real time. It provides detailed information about local ordering, bond distances (with resolution of the order of the hundredth of Å), and coordination numbers. The combination of *in situ* X-ray characterization and DFT calculations provides a unique means to determine the atomic arrangement and bonding in molecules deposited at a surface and, more precisely, the initial surface reaction mechanism.[36,38–40] Based on these chemical and structural analysis tools, this paper sheds new light on three distinct phases of the ALD/MLD of TiS_2 ultrathin layers: the reaction of the precursors with the substrate and the creation of the interface, the growth of non-crystalline intermediate thiolates, and the crystallization upon the annealing step.

Experimental section

Thin film fabrication and post-annealing treatment

The detailed process for sample preparation has been reported previously.[28] Briefly, ALD/MLD growth of the hybrid organic–inorganic Ti-thiolate had been performed on a 100 nm thick thermal SiO_2 substrate using alternate pulses of precursors TDMAT and EDT in a controlled manner. Prior to deposition, the substrates were pretreated at 200 °C in a 100 sccm nitrogen flow for 30 minutes. The temperature of the substrate was 50 °C during the sample growth. The growth of 40 ALD/MLD cycles was followed by continuous thermal annealing and cooling under a 100 sccm flow of H_2(4%)/Ar(96%) gas at a ramp rate of 10 °C min^{-1} up to 500 °C.

Synchrotron experiment setup

In situ XAS measurements have been carried out at the SIRIUS beamline of SOLEIL synchrotron, France, using a custom-built portable ALD/MLD reactor.[41,42] This undulator-based beamline

utilizes two different monochromators, the double crystal monochromator (DCM) and the multilayer grating monochromator (MGM), and operates in the energy range of 1.2 to 13 keV with high energy resolution.[43,44] The beamline is equipped with a large and accurate 7-circle Newport diffractometer to host cumbersome dedicated sample environments for *in situ* characterization of samples by X-ray scattering, spectroscopy, and reflectivity. The ALD/MLD reactor was mounted on the heavy-duty tower of a six-axis Newport diffractometer at the SIRIUS beamline. The experimental setup allowed performing multiple complementary *in situ* X-ray techniques *i.e.*, XAS, X-ray diffraction (XRD), X-ray reflectivity (XRR), and X-ray fluorescence (XRF). Fluorescence from the sample was measured using a four-element silicon drift detector (Bruker XFlash QUAD 5040) (SDD) mounted at one of the flanges of the reactor with provisions for varying distances from the sample. A collimator focused on the center of the sample was used at the detector nose with a 20-micron Kapton window to protect it from the precursor/reactants of the reactor. The SDD detector was coupled with a four-channel xMAP DXP electronics provided by XIA. All XRF and fluorescence-XAS data were corrected by non-linearity prior to their analysis.[45] The scattered X-rays were measured using a 2D hybrid pixel detector (PILATUS 1M by Dectris) placed at one of the arms of the six-axis diffractometer. The path between the reactor and pixel detector was connected through a He filled tube with 20-micron Kapton windows.

In situ X-ray absorption near edge structure (XANES) and extended X-ray absorption fine structure (EXAFS) measurements were carried out at the Ti (4966 eV) and S (2472 eV) K-edges in fluorescence mode during the inorganic–organic film growth and the annealing/cooling process. The incidence angle at the sample was kept at 1.2°, which is above the critical angle of Si at 5 keV; this choice helps to minimize the substrate background, preserving bulk sensitivity at the same time. The DCM synchronized with the undulator gap in continuous mode was used to measure the spectra in a faster way. The higher-order harmonics at the S K-edge were rejected using B_4C-coated mirrors, and Pt-coated mirrors were used at the Ti K-edge for the same purpose. A reference TiS_2 powder sample (purchased from Merck™) was measured with the same beamline setup during the experiment.

XAS analysis

The XAS analysis was carried out using the Demeter package, which includes Athena and Artemis subroutines for data processing and analysis.[46] The standard data analysis procedure includes background reduction and Fourier transform to derive the $\chi(R)$ *versus* R spectra from the absorption spectra (using Athena software), generation of the theoretical EXAFS spectra starting from an assumed crystallographic structure, and finally fitting of experimental data with the theoretical spectra using the Artemis software. The k-ranges used in Fourier transforms were 3–10 $Å^{-1}$ and 2–8 $Å^{-1}$ at the Ti K-edge and S K-edge, respectively. The R-ranges used for fitting the data at the Ti K-edge and S K-edge were 1–3.0 Å and 1–3.5 Å, respectively. The amplitude reduction factors were obtained from the EXAFS fitting of the TiS_2 spectra. The coordination numbers, bond lengths and disorder factors were kept variable during the fitting. The linear combination fitting (LCF) method was also carried out using the Athena software. Further details are given in the ESI.†

XANES simulations

The XANES simulations were carried out using the finite difference method near edge structure (FDMNES) code. It is a fully relativistic DFT-LSDA code and can be used in finite difference method (FDM) mode to solve the Schrödinger equation in which the shape of the potential is free and avoid the muffin-tin approximation.[47] We used the FDMNES program to simulate the XANES spectra, taking as an input several realistic atomic arrangements at the surface calculated by DFT, as detailed in the next paragraph. The simulations of the Ti K-absorption edge were performed using the finite difference method. The simulation cluster used in this study consisted of over 200 atoms surrounding the central Ti, with a dimension of 9.0 Å. The cluster radius was optimized by progressively increasing its size until convergence was achieved. The simulated intensity entirely resulted from electric dipole transitions. The convolution parameters of the simulation were optimized interactively using the PyFitit software tool.[48] The final optimized convolution parameters were a maximum width of 18 eV, a center of 50 eV, and a width of 18 eV for the arctangent function, with E_{fermi} at 4972 eV and theoretical core hole widths from Krause *et al.*[49]

DFT simulations

To study the initial stage of the ALD/MLD growth process, self-consistent DFT calculations were performed using the Vienna *ab initio* simulation package (VASP).[50] The revised Perdew–Burke–Ernzerhof functional for solids (PBEsol)[51] within the generalized gradient approximation (GGA) were used in these calculations. The plane wave cutoff energy was set to 450 eV and the Gaussian smearing was 0.05 eV. The total energy and atomic force convergence thresholds were defined as 10^{-4} eV and 10^{-3} eV $Å^{-1}$. The substrates were cleaved from a totally relaxed alpha-SiO_2 crystal along the (0001) plane. A five-layered slab expanded to a 3 × 3 × 1 supercell together with 24 Å vacuum was enough to describe the reaction surface and avoid the spurious interaction between neighboring layers. The use of the alpha-SiO_2 crystal structure helps to reduce computational costs thanks to its smaller unit cell.[52–54] Although the use of crystalline substrates has found widespread use in modeling the surface structure in various atomistic force field and DFT computational studies,[55–58] it is important to note that this represents a theoretical model of silicon dioxide and may not perfectly replicate the actual amorphous SiO_2 structure. While our simulations offer valuable insights into the initial growth cycle, there might be some variations when compared to amorphous SiO_2. The Brillouin zone was sampled with the Monkhorst–Pack division scheme. The 8 × 8 × 8 and 1 × 1 × 1 k-point meshes were applied to the bulk alpha-SiO_2 primitive cell and the supercell. In all these calculations, the bottom 2 layers were fixed.

Results

The creation of the interface

The optimal ALD/MLD growth process aims to achieve the formation of a monolayer of a well-defined unique metallic species on the hydrogenated thermal SiO_2 surface during the first half-cycle. However, bonding with the substrate remains dependent on various process parameters, noticeably the substrate pretreatment temperature, which can favor, as exemplified in the case of silica beads, the formation of a monopodal (one substrate–metal bond per deposited metal atom) and a bipodal (two metal–substrate bonds per deposited metal atom) coordination mode or a mixture of the two.[59] The *in situ* analysis of the first half-cycle growth on a silicon wafer pretreated at 200 °C carried out during the present experiment allowed us to unveil the bonding of TDMAT with the surface. DFT simulations were performed for a monopodal model where the TDMAT molecules were connected with the SiO_2 surface through one oxygen atom. The simulated XANES spectra at the Ti K-edge are shown in Fig. 1a for the two different models along with the experimental spectrum of the first half-cycle. The simulated XANES spectrum from the mono-podal model was able to generate the pre-edge and post-edge features (a and e in Fig. 1); however, the doublet peak points c and d could not be reproduced. Moreover, the mono-podal simulation shows an additional shoulder at the edge (b), which is not observed in the experimental spectrum. The calculated bond lengths from the monopodal model for different potentials and configurations are reported in ESI Table S1.†

The calculated bond lengths, especially the Ti–O bond, are far more distant from the experimental Ti–O and Ti–N bond distances obtained from the EXAFS analysis of the half-cycle. This observation motivated us to try other configurations of the bonding and we found the bi-podal model to be the most suitable one. The bipodal model connects the TDMAT molecule with the SiO_2 substrate using two Ti–O bonds and these

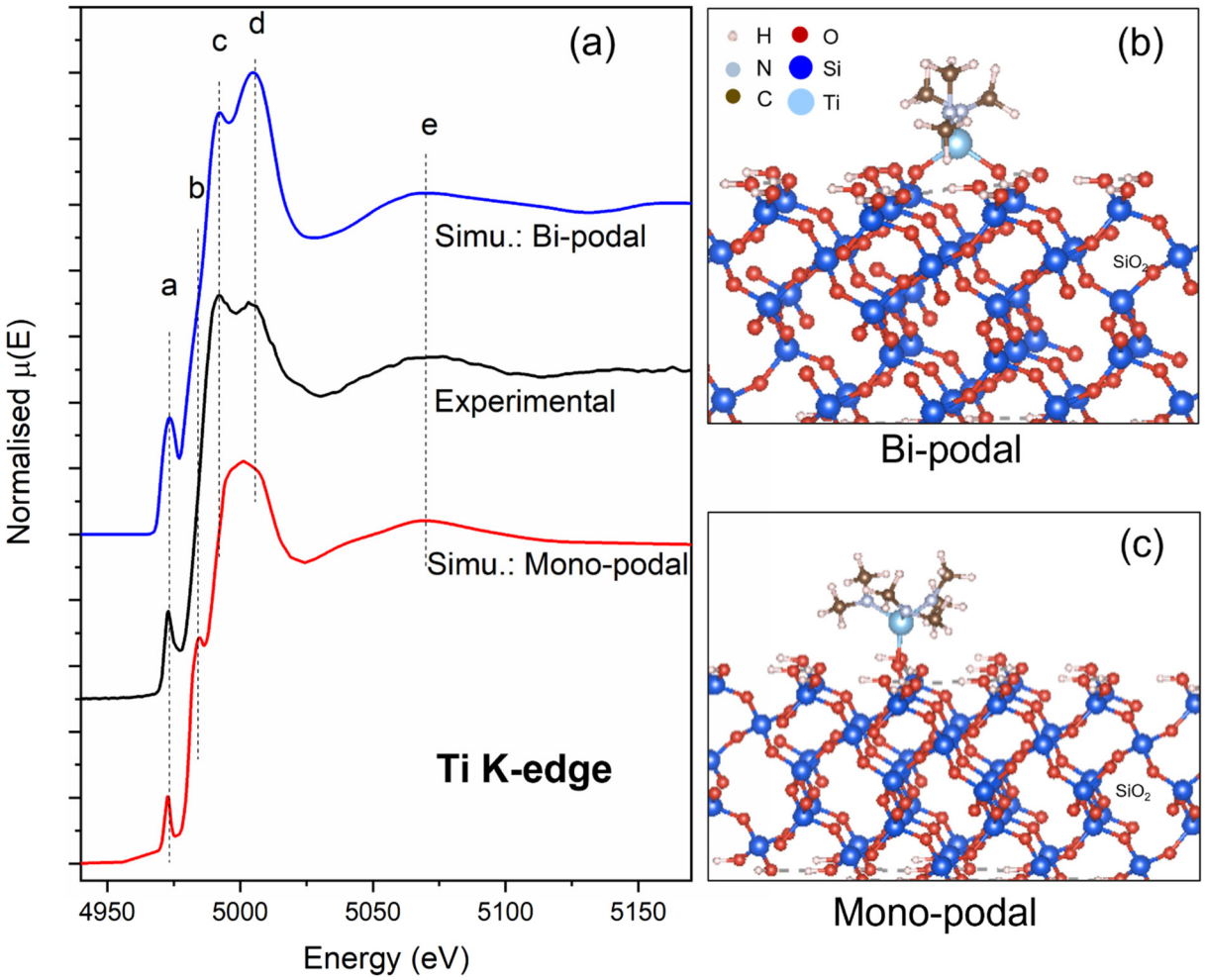

Fig. 1 (a) Experimental (middle) and theoretical simulated XANES spectra (top and bottom) of the ALD/MLD first half-cycle during the growth of metal–organic films. The two DFT optimized structures named the bi-podal model and the mono-podal model used for XANES simulations are shown in (b) and (c), respectively. The mono-podal model connects the TDMAT molecule to the substrate surface using one bridging oxygen while the bi-podal model connects TDMAT through two substrate oxygen atoms. The colors of the atoms in the model structures signify the following: red = oxygen, blue = Si, brown = carbon, sky blue = titanium, pink = hydrogen, and light-blue = nitrogen.

two oxygen atoms belong to two different Si atoms of the substrate. The simulated XANES spectrum was able to reproduce all the spectral features; however, the peak intensity is reversed compared to the experimental one. This discrepancy could be attributed to the various approximations employed during the simulations or the influence of the selected surface. To provide a more intuitive character of the stability of two structural configurations, the formation energy has been calculated using the following equation:

$$E_{\text{form}} = \frac{E_{\text{conf}} - \sum_i N_i E_i}{\sum_i N_i}$$

where E_{conf} is the total energy of two surface configurations, E_i is the energy per atom of the stable phase of each element and N_i is the number of elements in the super cell. The formation energy is −2.71 eV per atom and −3.06 eV per atom for the mono-podal and bi-podal models, respectively, indicating that the bi-podal configuration is more stable than the mono-podal one. The simulated XANES spectrum for the bi-podal model shown in Fig. 1a is able to generate all the major features (a–e) visible in the experimental spectrum of the half-cycle deposit. We took care to define the –OH groups per nm^2 at the surface before the calculation to mirror the experimental conditions (pre-annealing of the SiO_2 surface at 200 °C).[60]

The bipodal model for the first half-cycle was in excellent agreement with the observed preference for bipodal coordination on silica beads dehydroxylated at 200 °C, rather than the monopodal coordination observed for the same grafting reaction performed on silica beads dehydroxylated at higher temperatures. With the increasing pretreatment temperature of the substrate, the surface silanol reactive sites became isolated and sparse, therefore favoring monopodal over bipodal grafting.[59] Simulation of the MLD (second half) cycle is very challenging due to the involvement of large precursor molecules, interacting weakly and strongly with the three-dimensional partially known surface. These aspects are problematic for DFT due to the requirement of large simulation cells, weak chemical interactions, and unknown substrate surfaces. Therefore, we limited our work to the *ab initio* modeling of the first half-cycle.

The ALD/MLD growth

The normalized XANES spectra at the Ti K-edge during the growth of the metal–organic film are shown in Fig. 2a. The XANES spectra show two interesting changes as a function of the ALD/MLD cycle number. The first change can be observed

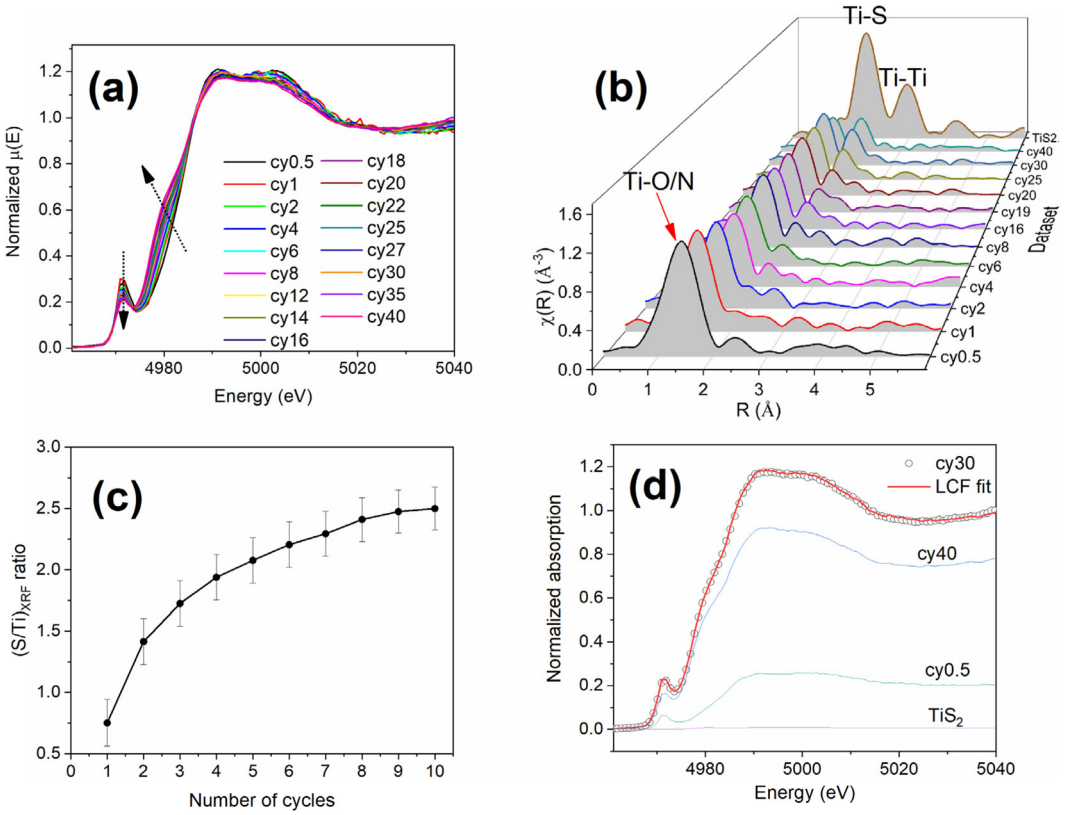

Fig. 2 (a) Normalized XANES spectra of the ALD/MLD cycles at the Ti K-edge. (b) Fourier transform EXAFS spectra recorded at various ALD/MLD cycles at the Ti K-edge. The Fourier-transformed spectra shown here are phase uncorrected and show coordination peaks at relatively lower distances than the actual bond lengths. (c) S/Ti ratios of the initial ten ALD/MLD cycles, calibrated using the XPS results. (d) Representative LCF of XANES spectra and the contribution of different components.

at the pre-edge at around 4972 eV. The pre-edge features of the K-edge XANES spectra of 3d transition-metal compounds were assigned to the electric dipole (1s → np) and quadrupole (1s → 3d) transitions. However, the intensity contribution of the quadrupole transitions was minor due to the orbital symmetry restrictions,[61] and the pre-edge features were therefore in most cases assigned to 1s electron excitation into p–d hybridized orbitals. The pre-edge feature intensity depended mainly on coordination, symmetry, and bond angles.[61] It has been observed that centrosymmetric coordination *i.e.*, octahedral coordination shows less hybridization compared to non-centrosymmetric coordination (tetrahedral coordination). A systematic decrease in the pre-edge intensity can be observed when the deposition proceeds from the first cycle to cycle 40. The initial intense pre-edge is related to the tetrahedrally coordinated TDMAT molecule grafted to the substrate. The optimized model for the first half-cycle corroborates this observation. As the ALD/MLD cycles proceed, more sulfur or carbon species surround the Ti atoms, which leads to an increase in the average coordination number and coordination symmetry of the Ti atoms, hence the pre-edge peak intensity decreases.

The second notable variation as a function of the ALD/MLD cycle number is shown by a spectral feature (a shoulder at 4980 eV) on the rising part of the absorption edge, which keeps growing during the deposition. This shoulder is attributed to the transition of Ti 1s electrons to unoccupied Ti 4p/S 3d hybridized orbitals.[62] This feature (which becomes a peak in crystalline materials) is characteristic of transition metal chalcogenides and is normally absent or negligible in titanium oxides.[63,64] The increase in the intensity of the shoulder with increasing cycle number further confirms the progressive increase of sulfur around the Ti atoms, as the ordered distribution of sulfur contributes to the constructive interference in multiple scattering, resulting in its higher amplitude.[64]

The contribution of the sulfur around the Ti atoms can also be seen in the Fourier transformed EXAFS spectra as a function of the ALD/MLD cycle number in Fig. 2b. The coordination peak at 1.5 Å in the Fourier transform spectrum corresponds to the first neighbor's shell. The Fourier transform spectrum of a TiS_2 standard is also included to better index the coordination peaks from the different neighboring shells in the sample spectra. The first peak for the half cycle, which is absent in TiS_2, originates from the contribution of two oxygen atoms at 1.90 Å coordinated with the substrate and two nitrogen atoms at 1.91 Å coordinated with the $-NMe_2$ group of the TDMAT precursors. The coordination peak related to the Ti–S bonds at around 2 Å starts appearing after a few ALD/MLD cycles only. One can see that the coordination peak related to the Ti–S bonds is continuously increasing in amplitude while the Ti–O/N peak is decreasing. The metal–organic film (cy40) shows a significant contribution of S around Ti. The absence of a coordination peak corresponding to the next nearest neighbor (Ti–Ti) at around 3 Å (Fourier transform spectrum of TiS_2) for all the ALD/MLD cycles indicates the very short-range character of atom ordering in the metal–organic film.

The (S/Ti) ratio obtained from the XRF measurements during the ALD/MLD cycles for the initial 10 growths is shown in Fig. 2c. The ratio was calibrated using X-ray photoelectron spectroscopy (XPS/HAXPES) data of the reference stoichiometric TiS_2 sample.[65] The absence of Ti–S coordination peaks during the very first cycles in the Ti K-edge Fourier transform EXAFS spectra can be understood through Fig. 2c, where the ratios of the initial 10 cycles are shown, while the ratios of the full growth up to 40 cycles are presented in ESI Fig. S3.† A similar S/Ti ratio has been previously reported for the growth of 60 cycles of ALD/MLD.[65] The small S/Ti ratio for the initial few cycles indicates a very small number of sulfur back scatterers; therefore, the Ti–S bonds are below the detection limit of the technique at the Ti K-edge.

We also note that the first Ti–O/N peak is always present up to the highest cycles, even if its intensity decreases with the cycle number. This suggests the presence of a fraction of Ti atoms not reacting or interacting with S in the metal–organic film, which does not yield a covalent or a dative bond between S and Ti, respectively, and remains in the local structure similar to the one of the first cycles. The presence of a fraction of such titanium atoms is in agreement with the incomplete surface reaction advancement during the ALD/MLD process modeled in our previous work.[28]

The LCF method involves fitting a linear combination of reference spectra of known chemical species to the experimental XANES spectrum in order to determine the relative contributions of each species.[46] LCF was used to identify the contributions of the different chemical species present in the samples during growth and annealing. The representative LCF for ALD/MLD cycle 30 is shown in Fig. 2d, with the contributions of the different components. The reference components used for LCF were able to reproduce the XANES spectra. The selection of the different components for LCF is described in the Discussion section.

The normalized XANES spectra at the S K-edge for the different ALD/MLD cycles are shown in Fig. 3 along with that

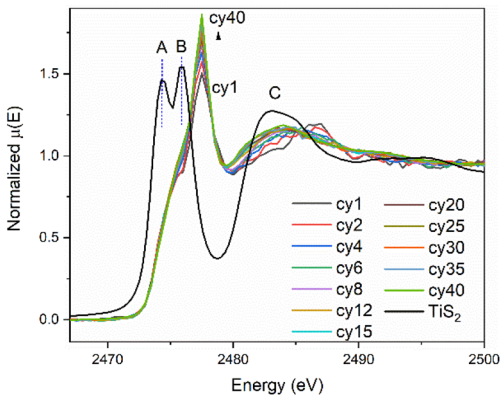

Fig. 3 The initial few cycles show small contamination (at around 2490 eV) of residual sulfur in the growth chamber. The XANES spectrum obtained prior to the growth cycles was used to remove this contamination.

of the reference spectrum of crystalline TiS_2. Here, we can detect a S signal and acquire a spectrum from cycle 1 (cy1), although this signal is very low in the first cycles (the difference in amplitude cannot be appreciated in the figure since the spectra are normalized; however, one can observe higher noise for the first cycles). The absorption spectra without normalization at the S K-edge are shown in ESI Fig. S4.† The two peaks A and B in TiS_2 are induced by the strong hybridizations between the Ti 3d and sulfur 3p states and can be assigned to the transitions to the t_{2g} and e_g bandlike states.[64] The broad feature C is induced by the hybridization between the sulfur 3p states and Ti 4s and 4p states.[62] The t_{2g} and e_g bandlike states are formed in crystalline TiS_2 due to the formation of narrow bands. It is evident from the figure that the XANES spectra of the metal–organic films are completely different from those of TiS_2. It has been previously reported that in metal–organic films, the S K-edge energy moves to higher energies as the sulfide bonding environment shifts from metallic/covalent to ionic.[66] In addition, the absence of a doublet peak similar to that of TiS_2 indicates a lack of long-range ordering in the metal–organic film. A systematic increase of the white line peak intensity at around 2477 eV is observed with increasing ALD/MLD cycle number. The increase in the white line intensity is related to the availability of more partially/unoccupied allowed states for the electron transition.[64,67] Apart from this clear difference in the white line, the shapes of all the S K-edge spectra were similar from cycle 1 to cycle 40, suggesting a similar S bonding and local environment of S and rather different from that of TiS_2. A minor change can also be observed at the right of peak C for some of the initial growth cycles (cy1 and cy2) with a peak at around 2487 eV probably due to surface contamination of the substrate; however, the contribution of the signal from this contamination is small (<1%) as can be seen in Fig. S4 and S5.†

We note here that the quantitative analysis of both the Ti K-edge and S K-edge spectra shown in this paragraph brings about new information on the ALD/MLD growth of these metal–organic films, which was not available before nor accessible *via* other techniques.

The annealing and cooling step

As mentioned above, the annealing step was expected to transform the metal–organic amorphous film into a crystalline film. The Ti-thiolate films were annealed under $Ar/H_2(4\%)$ gas to a moderate temperature (500 °C). The XANES and EXAFS measurements were carried out during the annealing and cooling of the sample to understand the process of transition from amorphous Ti-thiolate to crystalline TiS_2. The annealing was performed inside the ALD/MLD reactor directly after the growth, avoiding any contact with air (and spectrum contamination) related to sample transfer. The selective XANES and Fourier transform EXAFS spectra at the Ti and S K-edges for 40-cycle ALD/MLD are shown in Fig. 4 for the metal–organic film (cy40), annealed at 500 °C (cy40T500) and after cooling

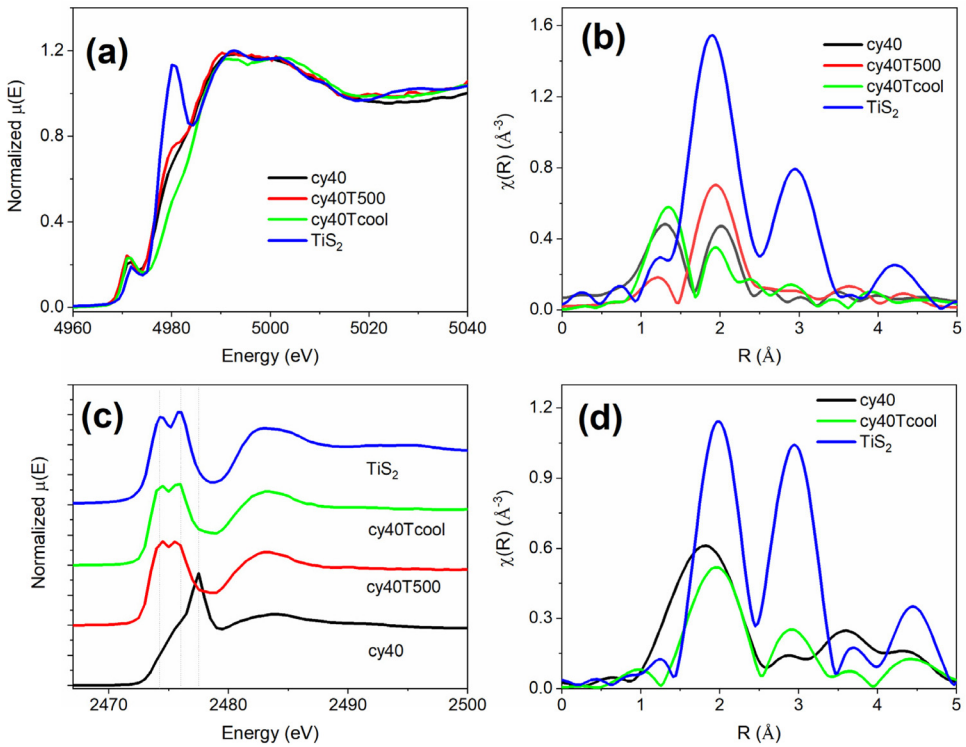

Fig. 4 Normalized XANES spectra of the Ti-thiolate (cy40), the Ti-thiolate film annealed at 500 °C (cy40T500), and the spectrum recorded after cooling (cy40Tcool) along with that of the standard TiS_2 at the (a) Ti K-edge and (c) the S K-edge. The respective Fourier transform EXAFS spectra are shown in (b) and (d).

(cy40Tcool). The XANES and Fourier transform EXAFS spectra of TiS_2 recorded in the same experimental setup are also included in Fig. 4.

In the Ti K-edge XANES spectra shown in Fig. 4a, the pre-edge peak at around 4972 eV is relatively higher for the Ti-thiolate and annealed samples in comparison with that of TiS_2; however, the annealed sample shows a relatively higher intensity of the pre-edge peak compared to the Ti-thiolate. It has been previously mentioned while discussing the growth results that the intensity of the pre-edge peak depends on the coordination, symmetry, and bond angles. The relatively higher intensity of the annealed sample was due to the relatively large thermal vibrations at higher temperatures (500 °C).[68] However, the pre-edge peak intensity remained the same even after cooling. This higher intensity after the cooling of the sample was due to the loss of sulfur after the annealing, which probably distorted the local coordination of Ti from perfect octahedral in TiS_2 to distorted octahedral.[61] A more substantial change can also be observed in the absorption edge shoulder/peak at around 4980 eV. This feature is due to the presence of S around the Ti atoms in an octahedral configuration and increases upon annealing. In crystalline TiS_2, the shoulder becomes a peak. The intensity of the shoulder also depends on the thickness (or the ALD/MLD cycle), as has been reported previously when comparing the cy40 and cy80 ALD/MLD samples.[28] However, this shoulder decreases in amplitude while cooling the samples inside the reactor, which is probably due to the loss of sulfur. Direct evidence of sulfur loss is given in Fig. S4 of the ESI,† where the non-normalized S K-edge X-ray absorption spectra reveal a reduction in the intensity of the annealed spectrum (cy40T500) and a further decrease in the intensity of the cooled spectrum (cy40Tcool). The loss of sulfur can also be observed in Fig. S6† through the recorded S/Ti ratio during the annealing and cooling processes. It has been observed that the samples removed immediately from the chamber after annealing show a relatively higher shoulder peak compared to the one kept inside the reactor to cool.[28]

The observations made through the XANES spectra are also mirrored in the Fourier transform spectra shown in Fig. 4b. The Ti-thiolate sample shows two coordination peaks at 1.4 Å and 2.1 Å (phase uncorrected spectra) corresponding to Ti–O/N at 1.90 Å and Ti–S at 2.45 Å coordination shells, respectively. The decrease in the coordination peak at 1.4 Å and the increase in the coordination peak at 2.1 Å can be seen after the annealing and give a direct indication of the crystallization of TiS_2, or at least of the creation of a local environment with TiS_2 symmetry, where the bonds between Ti and elements different from S are minimized. The Fourier transform spectrum of the cooled sample again shows a decrease in Ti–S coordination and an increase in Ti–O/N coordination, possibly attributed to the loss of sulfur from the sample. The fitting results at the Ti K-edge are shown in Table S2 of the ESI† and bond lengths are plotted in Fig. S7.†

The normalized XANES spectra at the S K-edge are shown in Fig. 4c for Ti-thiolate (cy40), annealed (cy40T500), and after cooling (cy40Tcool) along with that of standard TiS_2. The spectrum of the sample after annealing shows important changes with respect to the one of the Ti-thiolates and presents close similarity with TiS_2 and its line shape remains the same even after cooling. A small difference can be observed in the widths of the t_{2g} and e_g peaks, possibly due to a lower degree of long-range ordering or the effect of the polarized beam due to the preferred orientation in the samples compared to polycrystalline TiS_2. The Fourier transform spectra at the S K-edge shown in Fig. 4d corroborate the XANES observations. The Ti-thiolate shows a relatively broad first coordination peak at 1.9 Å, contributed by S–C, S–S, and S–Ti coordination. However, the spectrum of the annealed and cooled sample (cy40Tcool) shows complete similarity with TiS_2 in the position of the peaks, with reduced coordination peak intensity. The Fourier transform of the EXAFS spectrum for cy40T500 is absent in Fig. 4(d) due to the time constraints of the beamtime. Nevertheless, the close similarity of the XANES profiles shown in Fig. 4(c) for the cy40T500 and cy40Tcool spectra indicates a comparable coordination geometry between the two and suggests minor local changes upon the cooling step for the S atoms remaining in the sample. The S K-edge Fourier-transformed XAS spectrum for the cy40Tcool sample shows that at least two coordination shells around S are well distinguishable, suggesting that the material is not any more amorphous, but it shows some ordering beyond the nearest neighbors. It is however interesting to note that the amplitude difference of the two coordination peaks at 2.0 Å and 3.0 Å corresponding to S–Ti and S–S coordination, respectively, is small in the TiS_2 standard, while it is much bigger in the cy40cool sample. This observation corroborates the formation of a partly ordered crystalline atomically thin stack of TiS_2 observed through TEM.[28] Additional DFT calculations based on molecular dynamics and XANES simulations were also performed to evaluate possible variations in the spectra line shapes in amorphous TiS_2 and to address the degree of ordering in our annealed samples (see the ESI†). The result is that the crystalline TiS_2 structure is more effective than the amorphous ones in simulating the XANES spectra for the annealed samples.

Noteworthily, the S K-edge XANES spectrum, after annealing, shows a close similarity with TiS_2 while this is less true at the Ti K-edge. This observation suggests that all the remaining S atoms after the annealing have local coordination, as in crystalline TiS_2; however, not all the Ti atoms have local coordination like TiS_2. The chemistry underlying this observation will be further addressed in the Discussion section.

Fig. S6 in the ESI† shows the S/Ti ratio alongside the individual fluorescence from the Ti and S Kα lines during the annealing and cooling processes. The ratio distinctly illustrates the loss of sulfur during the annealing process. Furthermore, a smaller decrease can be observed after cooling, which corroborates the XANES observations discussed earlier. Similar behavior was also reported for 80 ALD/MLD cycles in our previous report, where the loss of S was also observed using diffuse reflectance infrared Fourier transform spectroscopy through chemical modeling on silica beads during the annealing treatment of a 2-cycle ALD/MLD Ti thiolate.[65]

Discussion

In order to summarize the results obtained in the three steps of sample growth (creation of the interface, deposition of the Ti thiolate, and annealing) and to confirm the observations made based on the EXAFS and XANES quantitative analyses, we revisit here the whole process in the light of the LCF approach discussed in the ESI.† This approach aims at

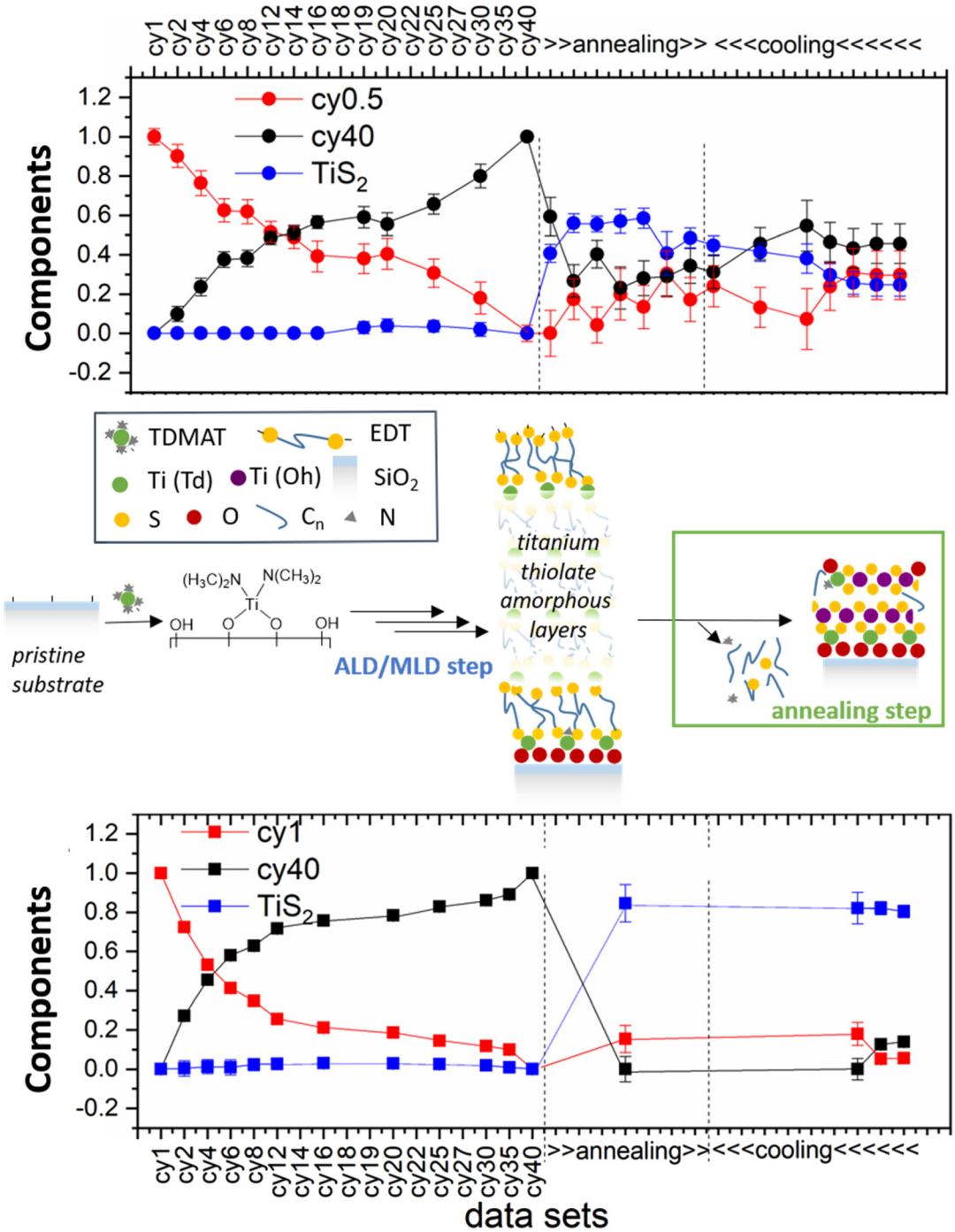

Fig. 5 LCF results during the growth and heat treatment at (top) the Ti K-edge and (bottom) the S K-edge. The annealing and cooling regions correspond to different temperatures under a 100 sccm flow of H_2(4%)/Ar(96%). (middle) The schematic overview of the whole ALD/MLD + annealing process interpreted through the XAS studies is reported here. The first step shows the first ALD pulse, where the Ti precursor connects to the hydrogenated SiO_2 substrate through a bi-podal coordination. The second step shows the potential structure after the complete growth of the thiolate film, which has contributions from oxygen in the initial cycle, an intermediary thiolate film with short-range ordering. The third step presents a simplified version of the final film, which is a TiS_2 film with the presence of an oxygen interlayer at the interface between the film and substrate. Additionally, there is a possibility of Ti coordination with nitrogen, apart from the targeted TiS_2 structure.

offering a comprehensive understanding of the growth process and the chemical reactions taking place at the various stages. It successfully validates the two-step synthesis approach, which entails distinct growth and crystallization steps. LCF was carried out at the Ti- and S-K edges on the XANES and EXAFS spectra using three components, which were sufficient to fit the spectra recorded during the growth and annealing followed by cooling. As we have seen from the fitting results of the Fourier transform, the Ti and S atoms have Ti–O/N, Ti–S, and S–Ti coordination; therefore, the XAFS spectra of the initial cycle (half ALD/MLD cycle (cy0.5) at the Ti K-edge and the first ALD/MLD cycle (cy1) at the S K-edge) and the final target structure, TiS_2, are the best suited to be used as LCF components. It is noted here that the initial cycle chosen for the Ti K-edge is a half ALD/MLD cycle (cy0.5) where the contribution of S is absent and for which the DFT optimized structure is available. The Ti-thiolate (cy40), an intermediate phase, is chosen as the third component for LCF, representing the amorphous character before the annealing step. The results of the LCF at the Ti and S K-edges for all growth steps are shown in Fig. 5 (top and bottom, respectively). A scheme of the chemical reactions underlying the whole process is shown in the same figure. The evolution of the components' weight during the growth process is similar for Ti and S with the continuous decrease of the initial ALD/MLD cycle corresponding to Ti–O/Ti–N coordination for Ti and S–C coordination around S, and the continuous increase of cy40 (Ti-thiolate) corresponding to the formation of the metal–organic film. The absence (values within the error limits) of any TiS_2 contribution was already observed before the annealing. This observation is in line with the XANES and EXAFS results shown in the previous section. The appearance of TiS_2 starts abruptly with the annealing of the sample with a slightly different behavior at the Ti and S K-edges. The LCF at the S K-edge shows that about 80% of the sulfur is in the TiS_2 phase and there is a small component that remains in a configuration like the one in the initial cycle. This is in good agreement with the XPS results reported in the previous paper (76% of the sulfur was incorporated in the TiS_2 phase).[28] However, at the Ti K-edge, about 60% of the total Ti coordination is similar to that of TiS_2, and a large amount of Ti still remains coordinated with oxygen or nitrogen, which corroborates the previously reported HAXPES results. In fact, HAXPES analysis carried out on samples after annealing showed that part of the titanium (45%) was still bonded to oxygen (not to nitrogen, which was not detected). This amount corresponds to the titanium oxides formed at the interface with SiO_2 and at the top surface after exposure to air (we note here that the Ti–O and Ti–N coordination could not be distinguished using XAS only, but they are distinguishable using HAXPES).

This result confirms the difference observed between the Ti K-edge XANES and the S K-edge XANES in the previous section. The overall data suggest the following interpretation of the results.

Upon annealing and following cooling, the evolution of the material can take two parallel and simultaneous paths: (1) formation of TiS_2, as clearly shown by the S K-edge data, (2) loss of S and formation of "S-free" Ti compounds similar (but probably not identical) to the one present at the beginning of the growth. The Ti K-edge data show that, finally, the material is a mixture of TiS_2 and these "S-free" Ti compounds. These "S-free" compounds also include the 2 nm thick interlayer observed in TEM between the wafer substrate and the deposit,[28] which is around 13% of the total thickness of the film, as well as undercoordinated titanium centers, which include the nitrogen-bearing species, also observed in the modeling studies performed on silica beads.[28] During the cooling, a marginally small decrease in TiS_2 contribution was observed in the S environment compared to a significant variation in the Ti environment, resulting from the loss of sulfur while annealing and cooling.

The values and trend of the bond lengths and interatomic distances extracted from the quantitative analysis of the EXAFS data (see the ESI and ESI Fig. S7–S9†) agree with our picture of the whole growth process. All these quantitative considerations and key insights achieved on the ALD/MLD of TiS_2 would not have been possible by using alternative *in situ* techniques. In fact, the method used needs to simultaneously possess chemical selectivity, sensitivity to weak and short-range order, bulk sensitivity, capacity of penetration in a gas environment, and high resolution in measuring atom correlations and interatomic distances.

Conclusions

We performed a full quantitative analysis of the Ti and S K-edge XAS data collected *in situ* during the ALD/MLD growth and annealing procedure aimed at producing TiS_2 ultra-thin films. The results of this analysis shed new light on the chemical and structural mechanisms underlying the different steps of this innovative growth strategy.

As for the interface formation, coupling XAS analysis with DFT simulations allowed us to unveil that the bonding of the TDMAT molecule with the surface in the initial half cycle is preferentially bipodal for typical substrate pre-annealing temperatures. Understanding the interactions with the substrate since the very first metal pulse of the ALD process is key because ultrathin film growth requires productive and chemically controlled reactions at the interface between the substrate and the growing phase to quickly obtain full coverage. Our results show that the growth mechanism complies with the models at its earliest stage.

The quantitative *in situ* monitoring of the ALD/MLD growth allowed us to validate the principle of the 2-step synthesis, separating growth and crystallization. In fact, an amorphous Ti-thiolate, characterized by a local structure clearly different from the one of TiS_2, is formed at the end of the deposition process. We also found out that S incorporation is strongly reduced during the first cycles and progressively increases with deposition. Moreover, a fraction of Ti atoms not fully coordinated to S (*e.g.*, not in octahedral coordination) and co-

ordinated with N or O is present at any stage of the ALD/MLD process even with decreasing concentration.

As for the annealing step, we gave quantitative evidence of the pursued transformation of the Ti-thiolate into TiS_2. Virtually all S atoms, after the annealing, were incorporated into a TiS_2 structure which showed a nanocrystalline characteristic, with atomic ordering at least up to the second neighbor's shell of S, despite the growth on an amorphous silica top layer. This can be considered an essential token of the success of the approach employed. Nonetheless, we showed that annealing is a critical step because it induces concomitant crystallization and S loss, and that the final product of the 2-step growth process is a mixture of nanocrystalline TiS_2 and of a S-free compound, suggesting avenues of improvement to produce an "ideal" two-dimensional crystalline TiS_2 without any other by-products.

Author contributions

Ashok Kumar Yadav: methodology, software, formal analysis, validation, writing – original draft, and writing – review & editing. Ma Weiliang: methodology, formal analysis, validation, visualization, software, and writing – review & editing. Petros Abi Younes: methodology, formal analysis, and writing – review & editing. Gianluca Ciatto: conceptualization, supervision, validation, project administration, funding acquisition, resources, and writing – review & editing. Nicolas Gauthier: conceptualization, supervision, and writing – review & editing. Evgeniy Skopin: conceptualization, supervision, and writing – review & editing. Elsje Alessandra Quadrelli: conceptualization, supervision, project administration, funding acquisition, resources, and writing – review & editing. Nathanaelle Schneider: conceptualization, supervision, project administration, funding acquisition, resources, and writing – review & editing. Hubert Renevier: conceptualization, supervision, project administration, funding acquisition, resources, and writing – review & editing.

Conflicts of interest

There are no conflicts to declare.

Acknowledgements

The financial support for this work was provided by the ANR project ANR-18-CE09-0031. The Ph.D. work of P. A. Y. was financed by the Labex MINOS (ANR-10-LABX-5501). The experiment at the SIRIUS beamline benefited from the SOLEIL beam time allocation no. 20190732 and 20200683.

Notes and references

1 F. Flamary-Mespoulie, A. Boulineau, H. Martinez, M. R. Suchomel, C. Delmas, B. Pecquenard and F. Le Cras, *Energy Storage Mater.*, 2020, **26**, 213–222.
2 B. Radisavljevic, A. Radenovic, J. Brivio, V. Giacometti and A. Kis, *Nat. Nanotechnol.*, 2011, **6**, 147–150.
3 V. Pore, M. Ritala and M. Leskelä, *Chem. Vap. Deposition*, 2007, **13**, 163–168.
4 M. S. Whittingham, *Science*, 1976, **192**, 1126–1127.
5 M. S. Whittingham, *MRS Bull.*, 2021, **46**, 168–173.
6 M. S. Whittingham, *Nat. Energy*, 2021, **6**, 214–214.
7 S. Li, J. Liu and B. Liu, *J. Power Sources*, 2016, **320**, 322–331.
8 A. Chaturvedi, P. Hu, V. Aravindan, C. Kloc and S. Madhavi, *J. Mater. Chem. A*, 2017, **5**, 9177–9181.
9 B. Tian, W. Tang, K. Leng, Z. Chen, S. J. R. Tan, C. Peng, G.-H. Ning, W. Fu, C. Su, G. W. Zheng, *et al.*, *ACS Energy Lett.*, 2017, **2**, 1835–1840.
10 C.-H. Lin, M. Topsakal, K. Sun, J. Bai, C. Zhao, E. Dooryhee, P. Northrup, H. Gan, D. Lu, E. Stavitski, *et al.*, *J. Mater. Chem. A*, 2020, **8**, 12339–12350.
11 J. Zhou, C. Zhu, Y. Zhou, J. Dong, P. Li, Z. Zhang, Z. Wang, Y.-C. Lin, J. Shi, R. Zhang, *et al.*, *Nat. Mater.*, 2023, **22**, 450–458.
12 R. Mas-Balleste, C. Gomez-Navarro, J. Gomez-Herrero and F. Zamora, *Nanoscale*, 2011, **3**, 20–30.
13 M. Mattinen, M. Leskelä and M. Ritala, *Adv. Mater. Interfaces*, 2021, **8**, 2001677.
14 J. Cai, X. Han, X. Wang and X. Meng, *Matter*, 2020, **2**, 587–630.
15 Y. Kim, W. J. Woo, D. Kim, S. Lee, S.-m. Chung, J. Park and H. Kim, *Adv. Mater.*, 2021, **33**, 2005907.
16 G.-H. Park, K. Nielsch and A. Thomas, *Adv. Mater. Interfaces*, 2019, **6**, 1800688.
17 H. Zhang, T. van Pelt, A. N. Mehta, H. Bender, I. Radu, M. Caymax, W. Vandervorst and A. Delabie, *2D Mater.*, 2018, **5**, 035006.
18 B. Chatmaneerungcharoen, M. Fraccaroli, F. Martin, C. Guedj, E. Nolot, D. Rouchon, N. Vaxelaire, R. Templier, A. Grenier, A.-M. Papon, *et al.*, *Chem. Mater.*, 2022, **34**, 5842–5851.
19 J. Dendooven and C. Detavernier, *Atomic layer deposition in energy conversion applications*, 2017, pp. 1–40.
20 S. Cadot, O. Renault, M. Frégnaux, D. Rouchon, E. Nolot, K. Szeto, C. Thieuleux, L. Veyre, H. Okuno, F. Martin, *et al.*, *Nanoscale*, 2017, **9**, 538–546.
21 S. M. George, *Chem. Rev.*, 2010, **110**, 111–131.
22 T. Yoshimura, S. Tatsuura and W. Sotoyama, *Appl. Phys. Lett.*, 1991, **59**, 482–484.
23 J. Multia and M. Karppinen, *Adv. Mater. Interfaces*, 2022, **9**, 2200210.
24 B. H. Lee, M. K. Ryu, S.-Y. Choi, K.-H. Lee, S. Im and M. M. Sung, *J. Am. Chem. Soc.*, 2007, **129**, 16034–16041.
25 A. Sood, P. Sundberg, J. Malm and M. Karppinen, *Appl. Surf. Sci.*, 2011, **257**, 6435–6439.
26 Y. Zhao, L. Zhang, J. Liu, K. Adair, F. Zhao, Y. Sun, T. Wu, X. Bi, K. Amine, J. Lu, *et al.*, *Chem. Soc. Rev.*, 2021, **50**, 3889–3956.
27 X. Meng, *J. Mater. Chem. A*, 2017, **5**, 18326–18378.
28 P. Abi Younes, E. Skopin, M. Zhukush, L. Rapenne, H. Roussel, N. Aubert, L. Khrouz, C. Licitra, C. Camp, M.-I. Richard, *et al.*, *Chem. Mater.*, 2022, **34**, 10885–10901.

29 A. Roussey, P. Gentile, D. Lafond, E. Martinez, V. Jousseaume, C. Thieuleux and C. Copéret, *J. Mater. Chem. C*, 2013, **1**, 1583–1587.
30 O. Sneh and S. M. George, *J. Phys. Chem.*, 1995, **99**, 4639–4647.
31 L. Mathey, T. Alphazan, M. Valla, L. Veyre, H. Fontaine, V. Enyedi, K. Yckache, M. Danielou, S. Kerdiles, J. Guerrero, *et al.*, *J. Phys. Chem. C*, 2015, **119**, 13750–13757.
32 T. Alphazan, L. Mathey, M. Schwarzwalder, T.-H. Lin, A. J. Rossini, R. Wischert, V. Enyedi, H. Fontaine, M. Veillerot, A. Lesage, *et al.*, *Chem. Mater.*, 2016, **28**, 3634–3640.
33 L. Kuai, J. Li, Y. Li, Y. Wang, P. Li, Y. Qin, T. Song, Y. Yang, Z. Chen, X. Gao, *et al.*, *ACS Energy Lett.*, 2019, **5**, 8–16.
34 K. Devloo-Casier, K. F. Ludwig, C. Detavernier and J. Dendooven, *J. Vac. Sci. Technol., A*, 2014, **32**, 010801.
35 E. Skopin, L. Rapenne, J. Deschanvres, E. Blanquet, G. Ciatto, L. Pithan, D. Fong, M.-I. Richard and H. Renevier, *Phys. Rev. Mater.*, 2020, **4**, 043403.
36 Y. Lei, J. Lu, H. Zhao, B. Liu, K.-B. Low, T. Wu, J. A. Libera, J. P. Greeley, P. J. Chupas, J. T. Miller, *et al.*, *J. Phys. Chem. C*, 2013, **117**, 11141–11148.
37 S. D. Elliott, G. Dey, Y. Maimaiti, H. Ablat, E. A. Filatova and G. N. Fomengia, *Adv. Mater.*, 2016, **28**, 5367–5380.
38 A. Yadav, N. Padma, G. Ghorai, P. K. Sahoo, R. Rao, S. Banarjee, A. Rajarajan, P. Kumar, S. Jha and D. Bhattacharyya, *Appl. Surf. Sci.*, 2021, **565**, 150548.
39 Y. Lei, F. Mehmood, S. Lee, J. Greeley, B. Lee, S. Seifert, R. E. Winans, J. W. Elam, R. J. Meyer, P. C. Redfern, *et al.*, *Science*, 2010, **328**, 224–228.
40 L. R. Aramburo, E. de Smit, B. Arstad, M. M. van Schooneveld, L. Sommer, A. Juhin, T. Yokosawa, H. W. Zandbergen, U. Olsbye, F. M. de Groot, *et al.*, *Angew. Chem.*, 2012, **124**, 3676–3679.
41 M. H. Chu, L. Tian, A. Chaker, V. Cantelli, T. Ouled, R. Boichot, A. Crisci, S. Lay, M.-I. Richard, O. Thomas, *et al.*, *Cryst. Growth Des.*, 2016, **16**, 5339–5348.
42 R. Boichot, L. Tian, M.-I. Richard, A. Crisci, A. Chaker, V. Cantelli, S. Coindeau, S. Lay, T. Ouled, C. Guichet, *et al.*, *Chem. Mater.*, 2016, **28**, 592–600.
43 G. Ciatto, M. Chu, P. Fontaine, N. Aubert, H. Renevier and J. Deschanvres, *Thin Solid Films*, 2016, **617**, 48–54.
44 G. Ciatto, N. Aubert, M. Lecroard, C. Engblom, P. Fontaine, J.-M. Dubuisson, Y.-M. Abiven, P.-E. Janolin, J.-M. Kiat, Y. Dumont, *et al.*, *J. Synchrotron Radiat.*, 2019, **26**, 1374–1387.
45 G. Ciatto, F. d'Acapito, F. Boscherini and S. Mobilio, *J. Synchrotron Radiat.*, 2004, **11**, 278–283.
46 B. Ravel and M. Newville, *J. Synchrotron Radiat.*, 2005, **12**, 537–541.
47 O. Bunau and Y. Joly, *J. Phys.: Condens. Matter*, 2009, **21**, 345501.
48 A. Martini, S. Guda, A. Guda, G. Smolentsev, A. Algasov, O. Usoltsev, M. Soldatov, A. Bugaev, Y. Rusalev, C. Lamberti and A. Soldatov, *Comput. Phys. Commun.*, 2020, **250**, 107064.
49 M. O. Krause and J. H. Oliver, *J. Phys. Chem. Ref. Data*, 1979, **8**, 329–338.
50 G. Kresse and J. Furthmüller, *Phys. Rev. B: Condens. Matter Mater. Phys.*, 1996, **54**, 11169.
51 J. P. Perdew, A. Ruzsinszky, G. I. Csonka, O. A. Vydrov, G. E. Scuseria, L. A. Constantin, X. Zhou and K. Burke, *Phys. Rev. Lett.*, 2008, **100**, 136406.
52 J. Rimsza, R. Jones and L. Criscenti, *Langmuir*, 2017, **33**, 3882–3891.
53 C. Lombard, C. van Sittert, J. Mugo, C. Perry and D. Willock, *Phys. Chem. Chem. Phys.*, 2023, **25**, 6121–6130.
54 G.-M. Rignanese, J.-C. Charlier and X. Gonze, *Phys. Chem. Chem. Phys.*, 2004, **6**, 1920–1925.
55 B. Han, Q. Zhang, J. Wu, B. Han, E. J. Karwacki, A. Derecskei, M. Xiao, X. Lei, M. L. O'Neill and H. Cheng, *J. Phys. Chem. C*, 2012, **116**, 947–952.
56 M. Pfeiffer-Laplaud and M.-P. Gaigeot, *J. Phys. Chem. C*, 2016, **120**, 4866–4880.
57 J. W. Han and D. S. Sholl, *Phys. Chem. Chem. Phys.*, 2010, **12**, 8024–8032.
58 X. Wang, Q. Zhang, X. Li, J. Ye and L. Li, *Minerals*, 2018, **8**, 58.
59 V. Riollet, E. A. Quadrelli, C. Copéret, J.-M. Basset, R. A. Andersen, K. Köhler, R.-M. Böttcher and E. Herdtweck, *Chem. – Eur. J.*, 2005, **11**, 7358–7365.
60 L. Zhuravlev, *Colloids Surf., A*, 2000, **173**, 1–38.
61 T. Yamamoto, *X-Ray Spectrom.*, 2008, **37**, 572–584.
62 L. Zhang, D. Sun, J. Kang, H.-T. Wang, S.-H. Hsieh, W.-F. Pong, H. A. Bechtel, J. Feng, L.-W. Wang, E. J. Cairns and J. Guo, *Nano Lett.*, 2018, **18**, 4506–4515.
63 O. Šipr, A. Šimunek, S. Bocharov, D. Heumann and G. Dräger, *J. Synchrotron Radiat.*, 1999, **6**, 518–520.
64 M. F. Smith, K. Setwong, R. Tongpool, D. Onkaw, S. Naphattalung, S. Limpijumnong and S. Rujirawat, *Appl. Phys. Lett.*, 2007, **91**, 142107.
65 P. Abi Younes, A.-K. Yadav, M. Zhukush, V.-H. Le, H. Roussel, M.-I. Richard, C. Camp, K. Szeto, G. Ciatto, N. Schneider, E. A. Quadrelli, H. Renevier and N. Gauthier, *J. Vac. Sci. Technol., A*, 2023, **41**, 042403.
66 B. A. Anzures, S. W. Parman, R. E. Milliken, A. Lanzirotti and M. Newville, *Am. Mineral.*, 2020, **105**, 375–381.
67 Z. Huang, Z. Q. Liu, M. Yang, S. W. Zeng, A. Annadi, W. M. Lü, X. L. Tan, P. F. Chen, L. Sun, X. Renshaw Wang, Y. L. Zhao, C. J. Li, J. Zhou, K. Han, W. B. Wu, Y. P. Feng, J. M. D. Coey, T. Venkatesan and A. Ariando, *Phys. Rev. B*, 2014, **90**, 125156.
68 O. Durmeyer, E. Beaurepaire, J.-P. Kappler, C. Brouder and F. Baudelet, *J. Phys.: Condens. Matter*, 2010, **22**, 125504.